PHYSICAL REVIEW E VOLUME 56, NUMBER 6 DECEMBER 1997

Measurements of planar target heating by an intense lithium ion beam

J. E. Bailey,[1] J. J. MacFarlane,[2] P. Wang,[2] A. L. Carlson,[1] T. A. Haill,[1] D. J. Johnson,[1] P. Lake,[3] E. J. McGuire,[1] and T. A. Mehlhorn[1]
[1]*Sandia National Laboratories, Albuquerque, New Mexico 87185-1187*
[2]*Fusion Technology Institute, University of Wisconsin, Madison, Wisconsin 53706*
[3]*K-Tech Corporation, Albuquerque, New Mexico 87110*

(Received 2 May 1997; revised manuscript received 2 September 1997)

The heating of a planar multilayer (CH-Au-Al-CH) foil target by an intense lithium ion beam is measured using time-integrated spectroscopy of $K\alpha$ x-ray satellite emission from the Al layer. The time-resolved beam irradiance, kinetic energy, and focal spot size are simultaneously measured using lithium ions Rutherford scattered from the foil. The approximately 20 ns full width at half maximum, 10 MeV peak kinetic energy, Li^{3+} ion beam deposited up to 435 TW/g (±30%) in the Al layer. The peak electron temperature reached in the Al layer is estimated to be 38–43 eV by comparing the relative emission intensities from the He-like and Li-like Al with collisional-radiative-equilibrium (CRE) calculations. The data are used to examine one-dimensional radiation-hydrodynamic simulations that calculate the target plasma temperature and density using the measured beam parameters as input. It was found that a detailed CRE treatment of the atomic level populations and the line transport is essential for accurate calculations of the radiation loss from the ion heated target. Simulations that include such a treatment embedded within the radiation-hydrodynamic calculations are in good agreement with the data, within the experimental uncertainties. The methods developed here for observation and analysis of $K\alpha$ spectra provide a sensitive tool suitable for the more stringent examinations of intense ion beam-matter interaction models that will ultimately be required for light-ion driven fusion. [S1063-651X(97)03612-X]

PACS number(s): 52.58.Ei, 52.70.La, 52.40.Mj, 52.25.Nr

I. INTRODUCTION

Target heating with light ion beams is a promising method [1–3] for achieving inertial confinement fusion (ICF). Significant improvements in ion beam irradiance, beam emittance, and control over the beam kinetic energy are needed to achieve fusion. Reaching this goal will also require a robust predictive capability for intense ion beam–plasma interaction. The term ‘‘interaction’’ here includes the deposition of ion energy into the target, the hydrodynamic target motion, and the radiation generation and transport. The present status is that only extremely limited experiments validating radiation hydrodynamic models of ion beam target interaction have been reported in the high beam intensity regime. This paper describes experiments and simulations that are a step towards providing such tests.

The baseline approach to light ion fusion relies on an indirect-drive hohlraum configuration consisting of a gold sphere filled with low-density CH foam, with the actual ICF capsule at the center [4,5] of the sphere. The ions penetrate the gold wall and deposit their energy in the foam, stopping before they impact the capsule. The radiation from the CH plasma is confined by the gold hohlraum wall, providing a symmetrized bath of x rays that drives the capsule implosion. High-efficiency ICF implosions depend critically on knowledge of the ion range, since ions that are deposited too deeply inside the hohlraum target are likely to imprint asymmetries on the capsule, while if the ion range is shorter than expected, the hohlraum target mass will be larger than desired for maximum yield. Most of the ion stopping is provided by collisions of projectile ions with target electrons. Range shortening, along with a corresponding increase in the energy deposited per unit length (dE/dx), occurs as the target is heated. This is because free electrons resulting from target atom ionization contribute more to the stopping than an equal number of bound electrons. A review [6] of the concepts and available measurements of ion stopping in plasmas indicates that at present, the uncertainty in ion stopping calculations is approximately ±15%. Reduction of the ion range uncertainty is needed for more robust target designs and a credible attempt at achieving fusion. In addition, the radiation flux from the ion-beam-heated plasma inside the hohlraum depends on the plasma temperature, density, and composition. Accurate calculations of the radiation generation and transport require predictions of the plasma temperature and density evolution and self-consistent predictions of the atomic level populations. The complexity of such radiation hydrodynamic calculations, and the interrelationship between the ion range and the radiating target plasma created by the beam, motivates experiments aimed at testing models for the ion beam target interaction.

Experimental information on ion-heated targets has been limited by the difficulties encountered in producing high-power ion beams. Previous related experiments have measured ion slowing in a z pinch [7,8] or laser-produced plasma [9] that is created independent of the ion beam. The first experiments measuring range shortening in an ion-beam-generated plasma were conducted by Young *et al.* [10] using a ~50 TW/g deuteron beam. Later experiments [11] extended range shortening measurements to a ~200 TW/g proton beam. However, neither of these experiments included a measurement of the target temperature. Consequently, the calculations of range shortening that were compared with the data relied on radiation hydrodynamic simulations of the

1063-651X/97/56(6)/7147(12)/$10.00

plasma temperature and the resulting ionization distribution. Therefore, these experiments were extremely valuable, but they were unable to test simulations of the integrated ion beam deposition–radiation generation physics. The temperature of heavy-ion-beam produced plasmas has been spectroscopically measured [12,13] and compared with simulations, but the specific deposition was limited to ~0.3 TW/g and the resulting plasma temperatures were less than about 1 eV. In recent intense proton [14–16] and lithium [17] ion beam experiments with specific depositions up to 1600 TW/g the target temperature was measured, but in all these experiments a simultaneous measurement of the incident beam irradiance was inhibited by the use of target geometries that maximized the resulting temperature, at the expense of limiting diagnostic access. This again prevented tests of the ability to accurately model the ion beam–plasma interaction.

The unique feature of the present experiments is a simultaneous measurement of the incident beam intensity and the resulting target plasma temperature. An approximately 1.2 TW/cm^2, 10 MeV, 20 ns full width at half maximum (FWHM) Li^{3+} ion beam irradiates a CH-Au-Al-CH multilayer foil target, reaching a peak specific deposition of about 435 TW/g in the Al layer. A suite of diagnostics uses Rutherford-scattered beam ions (primarily from the Au layer) to measure the space- and time-resolved incident beam kinetic energy, irradiance, and focal spot size. The uncertainty in the measured absolute ion beam irradiance is estimated to be ±30%. The target temperature is measured using time-integrated $K\alpha$ x-ray satellite emission, produced when ion impact ionization creates K-shell holes in the Al. The $K\alpha$ technique was found to be a very sensitive tool for diagnosing ion heated plasmas, providing the capability to measure changes in the electron temperature of ~5% and in the ion beam irradiance of ~10%. The fact that the ion beam is continually heating the target during the time when $K\alpha$ x rays are generated also implies that the target temperature monotonically increases during this period. The $K\alpha$ features corresponding to low charge states are thus produced mainly early in time and the features corresponding to high charge states are produced mainly near the end of the pulse, when the temperature is the highest. This enabled us to determine that the peak electron temperature in the Al layer is 38–43 eV by comparing the relative intensity of satellites arising from the Li- and He-like aluminum charge states with collisional-radiative calculations. The sensitivity of the $K\alpha$ technique also enabled us to test the validity of one-dimensional (1D) radiation-hydrodynamic simulations of the target, using the measured beam properties as the simulation input. Detailed atomic energy level modeling embedded within the radiation-hydrodynamic code was used to provide accurate atomic populations and radiation transport. Comparisons of the detailed line-transport model with more traditional multigroup transport calculations showed that for the Al plasma conditions—optically thin continuum but optically thick lines—the multigroup model overestimates the radiation loss by a factor of 2–5. The detailed treatment used here was therefore essential to obtaining accurate results. The relative emission intensities of the simulated $K\alpha$ satellite features reproduce the experimental values reasonably well, although the simulated spectra are systematically somewhat underionized. Increasing the simulation input beam intensity by 25% gave excellent agreement, while an increase of 50% resulted in an overionized synthetic spectrum. This indicates that present models of the beam-target interaction, including models for both ion beam deposition and radiation generation and transport, are adequate to provide predictive capability for these experiments, given the ±30% uncertainty in the measured ion beam irradiance.

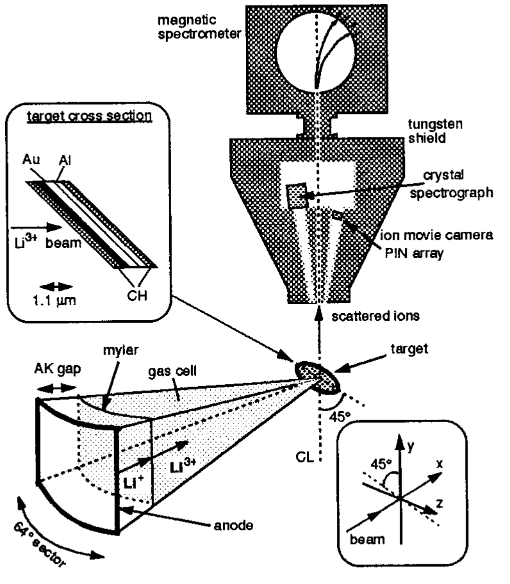

FIG. 1. Schematic diagram of the experiments. The diode is cylindrically symmetric about the center line CL, but only a 64° azimuthal sector is allowed to irradiate the target on axis. The target lies in the plane formed by the z axis and a line in the xy plane at 45°. Note that for clarity, only the top diagnostic suite is shown; more diagnostics are located below the target.

The methods developed here for observation and analysis of $K\alpha$ spectra provide a sensitive tool suitable for the further more detailed examination of models for higher power ion beam interaction with matter that will be required for light-ion driven fusion. Future experiments should use time-resolved spectroscopy and improved beam irradiance accuracy. However, as noted above, the charge state distribution progresses from low charge states early in the pulse to high charge states later. In addition, the intensity of each $K\alpha$ feature depends on the duration of the appropriate charge state's existence in the plasma, convolved with the beam intensity and kinetic energy in that time interval. These facts imply that the agreement with the present time-integrated data already provides some support for the time-dependent simulation fidelity.

II. ION BEAM MEASUREMENTS

In our experiments an applied-magnetic-field ion diode [18] converts the electrical power pulse from the Particle Beam Fusion Accelerator II (PBFA II) into an intense lithium ion beam. The cylindrically symmetric diode accelerates a radially directed singly ionized lithium beam across a ~2 cm anode-cathode (AK) gap (Fig. 1). The AK gap is insulated against electron losses by a 2–3 T magnetic field applied parallel to the cylindrical axis (see Ref. [18]). After acceleration, the beam enters a gas cell and is ballistically transported ~13 cm to the target located on the cylinder axis.

The beam is stripped into the Li^{3+} charge state upon penetration of the 2-μm-thick Mylar membrane that separates the AK gap from the 2 Torr argon gas cell and it remains approximately fully ionized when it impacts the target. The diode is divided into four 64° azimuthal sectors for diagnostic purposes. The beam from one 64° sector irradiates the planar foil target on the diode axis and the beam from the other three sectors is directed into a variety of other off-axis diagnostics to further evaluate the beam properties. The target is placed at a 45° angle with respect to the diode axis. The foil target consists of a CH-Au-Al-CH sandwich, with typical layer thicknesses 0.2 μm–0.5 μm–0.2 μm–0.2 μm, respectively. The lithium beam deposits only about 10% of its energy (at the 10 MeV peak incident kinetic energy) in this relatively thin foil. The target was kept thin compared to the ion range in order to minimize gradients and difficulties with beam diagnostic interpretation, at the expense of lower deposited beam energy. The CH layers are intended to retard the hydrodynamic expansion of the Au and Al layers. The Au layer provides the primary beam diagnostic, since about 95% of the total Rutherford-scattered ion signal results from the gold because of its high atomic number (Z) and density. The aluminum layer is chosen because its relatively simple $K\alpha$ spectrum provides a measure of the target temperature, as described below.

The ion beam incident on the planar foil targets was measured [19] with a time-resolved ion pinhole camera [20], an energy-resolved time-integrated ion pinhole camera [21,22], and a time-resolved magnetic spectrometer [23–25] that also has 1D spatial imaging capability. The time-resolved ion pinhole camera uses a 2D array of P-I-N diodes to record ions Rutherford scattered from the target and imaged through a 0.7-mm-diameter pinhole (magnification = 2). This diagnostic is considered to be the most accurate measure of irradiance because of the 2D imaging and the time resolution. The magnetic spectrometer also records Rutherford-scattered ions with a 2D P-I-N array, but in this case one dimension is used to measure the beam kinetic energy and the other provides 1D spatial imaging. Both time-resolved diagnostics are housed within a 1000 kg tungsten shield to reduce the noise induced in the P-I-N diodes by the hard x rays generated from electron losses in the diode. The energy-resolved ion pinhole camera uses a nuclear track recording plastic (CR-39) to record Rutherford-scattered ions imaged separately through six pinholes, with different filter thicknesses to provide energy bins. This instrument provides the best spatial information and quasitime resolution can be obtained, since the beam kinetic energy falls monotonically during the pulse.

We first use the magnetic spectrometer to determine the time-resolved beam kinetic energy (voltage) as a function of the horizontal position (z direction in Fig. 1). The 1D spatial imaging capability is important because the instantaneous beam kinetic energy varies with horizontal position by up to 10%. This is in addition to the instantaneous kinetic energy spread at any given target position, which is typically small early in the pulse but can rise to ±10% late in the pulse. Knowing the beam kinetic energy, we determine the incident particle current density and the focal spot size on the target from the time-resolved ion pinhole camera, correcting for the energy dependence of the Rutherford-scattering cross section and the time of flight from the target to the detector. The magnetic spectrometer is also used to determine the incident particle current density (integrated over the vertical spatial dimension), while the energy-resolved pinhole camera mainly provides a cross check on the primary time-resolved measurements. The measured lithium ion beam properties from PBFA II experiment 5851 are shown in Fig. 2. During the first 10 ns of the pulse the beam is essentially 100% Li^{1+} in the acceleration gap, impacting the target as Li^{3+}. Later, impurities appear in the beam, but they do not focus onto the target because of deflections in the applied magnetic field. The Li^{3+} irradiance shown in Fig. 2 is taken near the peak of the approximately Gaussian beam profile. The focal spot size measurements reported in Fig. 2 correspond to the dimensions of the beam FWHM measured perpendicular to the beam propagation direction. The actual beam spot in the foil plane is elongated in the vertical direction (y in Fig. 1) because of the 45° target tilt angle.

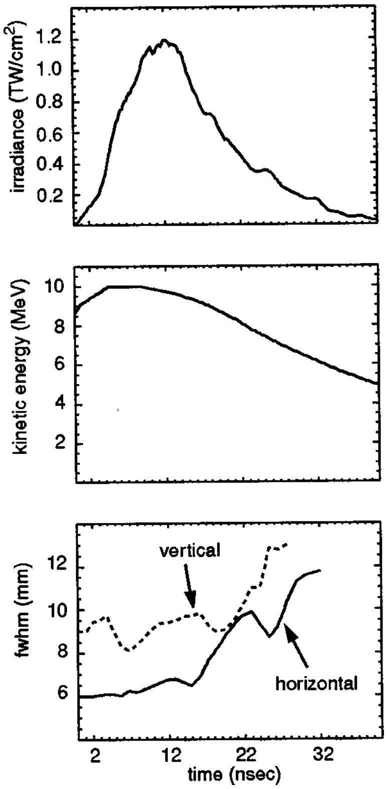

FIG. 2. Measured lithium ion beam properties from PBFA II experiment 5851. The beam irradiance is specified at the peak of the approximately Gaussian intensity distribution.

The Rutherford-scattering diagnostics measure the ion beam properties after the ions travel through the target. Thus, in order to determine the beam properties incident on the surface of the target, the energy lost by the beam ions in the target plasma must be taken into account. This loss depends on the target plasma temperature because of the range shortening effects mentioned above [6]. The temperature dependence of the energy loss in the hot target was taken into account using an iterative procedure. First the beam irradiance was determined using the cold stopping. Then the radiation hydrodynamic code described below was used to calculate the region-averaged target temperature for each material as a function of time. The irradiance was then re-

TABLE I. Processes leading to $K\alpha$ satellite transitions. Note that for clarity the examples refer to specific initial configurations, although in general a distribution of charge states and excited states will exist. For all cases the configuration after ion impact decays when a $2p$ electron fills the $1s$ hole.

Example description	Initial configuration	Configuration after ion impact
(A) Single ion impact ionization, hot Al target	$1s^22s^22p^2$ (C-like)	$1s2s^22p^2$ (B-like)
(B) Multiple ion impact ionization, hot Al target	$1s^22s^22p^4$ (O-like)	$1s2s^22p^2$ (B-like)
(C) Single ion impact ionization, hot Al target	$1s^22s^22p^23s$ (N-like)	$1s2s^22p^23s$ (C-like)
(D) Single ion impact ionization, hot Al target	$1s^22s2p$ (Be-like)	$1s2s2p$ (Li-like)

evaluated using the hot target dE/dx energy loss. This treatment increases the irradiance by 10–20% during the second half of the pulse after the target has heated up. This correction is relatively small, even though the target heating enhances the energy deposition by up to a factor of 4 (Sec. IV), because the energy lost in the thin foil target is a relatively small fraction of the incident beam energy.

The uncertainty in the incident beam properties is important because ultimately this limits the severity of the tests we can apply to our understanding of beam target heating. The irradiance data shown in Fig. 2 are an average over the magnetic spectrometer and movie camera results. The variation of the two measurements about the average is less than ±15% throughout the pulse, but we estimate [23–25] the absolute uncertainty to be approximately ±30%. The possibility of errors in the angular dependence of the incident beam is particularly important because of the $\sin^4\phi$ term in the Rutherford-scattering cross section. This concern is exacerbated if the beam current density is spatially nonuniform within the 64° sector that irradiates the target, since ions that are preferentially accelerated from either the top or bottom of the anode arrive at the target with greater or smaller incident angles, respectively. An array of Faraday cups located in one of the other sectors is used to verify that global nonuniformities are less than ±20%. The errors that result from other factors such as the target thickness, the P-I-N detector dead layer thickness, and the hot target dE/dx correction are each small, but their cumulative effect can be significant. In addition, although impurity ions are deflected from the target center by the magnetic field, it is difficult to measure the actual impurity ion flux reaching the center of the target because filter and target thicknesses chosen to optimize the lithium signal are sufficient to completely stop most impurities before they reach the P-I-N detectors. Therefore, we cannot rule out the possibility that impurity ions deposit energy in the target center up to the equivalent of approximately 10% of the total lithium beam energy deposition. Thus, it is difficult to reduce the uncertainty in Rutherford scattering ion beam intensity measurements below ±30%.

III. TARGET HEATING MEASUREMENTS

The response of the target to the ion beam heating is measured using Al $K\alpha$ x-ray satellite spectroscopy. $K\alpha$ satellite transitions appear when inner-shell ionization from the $n=1$ (K) shell of an atom is accompanied by simultaneous vacancies in the $n=2$ or $n=3$ (L or M) shells. The wavelength of the $1s$-$2p$ $K\alpha$ transition is sensitive to these extra vacancies because the screening of the nucleus experienced by the electron making the $1s$-$2p$ transition is reduced when there are fewer spectator electrons. Thus, the satellite lines are blueshifted with respect to the neutral-atom $K\alpha$ transition, with the amount of the blueshift increasing as the number of L- or M-shell vacancies increases.

$K\alpha$ satellites are observed when an atom embedded in a hot plasma undergoes simultaneous thermal ionization and bombardment with high-energy projectiles. For moderate plasma temperatures (10–100 eV), thermal ionization of medium-Z atoms such as aluminum produces L-shell vacancies. Energetic electrons or ions incident on a such a hot target produce $1s$ vacancies by inner-shell impact ionization, leading to emission of $K\alpha$ satellites as the $1s$ holes are filled. An example for an Al target atom initially in the C-like charge state is shown in Table I(A). After the inner-shell ionization, the $K\alpha$ transition occurs in the B-like ion. Such processes are responsible for $K\alpha$ satellites observed in solar and Tokamak spectra [26], they have been used to measure hot electrons in CO_2 laser experiments [27,28], and they were proposed [29] by Nardi and Zinamon as a means to measure the temperature of ion-heated plasmas. This diagnostic method relies on the emission of a characteristic satellite wavelength by each charge state, so that the target plasma charge state distribution can be determined from the relative intensity of the satellites. The plasma temperature can then be inferred from the ionization distribution, provided some information is available for the plasma density. The first experiments [14] exploiting $K\alpha$ satellites to diagnose an ion-beam-heated target were performed in 1990, although, as noted above, these experiments offered limited capability to test understanding of beam-heated matter because the incident ion beam was not simultaneously measured. Another type of $K\alpha$ satellite experiment uses thermal ionization in a hot plasma to produce L-shell holes and the satellite transitions are then observed in absorption using an x-ray backlighter. The use of this method in laser-produced and x-ray-heated plasma experiments has become widespread [30–34] in recent years and is presently considered to provide a robust (better than ±10% accuracy) temperature diagnostic in the 30–80 eV temperature range. These experiments are relevant to the present, ion-beam-produced, $K\alpha$ satellite measurements because they provide a database that is used to benchmark the complex atomic physics computer codes used to analyze the data.

The atomic physics calculations used to interpret the ion-induced $K\alpha$ satellite spectra must account for the term-dependent fluorescence yields, the charge state dependence of the inner-shell ionization cross sections, and resonant self-absorption. The analysis is further complicated by the fact that there is not a one-to-one correspondence between the $K\alpha$ satellite intensity distribution and the charge state distribution. Processes exist that cause transitions from different charge states to overlap. Multiple inner-shell ionization [35] is potentially important because of the finite probability that a beam ion creates one or more L-shell holes, in addition to the K-shell hole. The multiple and single ionization cross sections are comparable for ~10 MeV Li^{3+} projectiles incident on Al I–IV ions, but the multiple ionization cross section decreases rapidly as the target ionization increases because the target atom electrons are more tightly bound. Multiple ionization results in a transition that corresponds to one or more charge states above the usual, single-inner-shell-ionization $K\alpha$ satellite. An example of multiple ionization of an Al target atom initially in the O-like charge state is shown in Table I(B). In this example, two extra vacancies in the $2p$ shell are created in addition to the $1s$ inner-shell vacancy, and the resulting transition occurs in a B-like Al atom. This emission will overlap with the $K\alpha$ feature from single ionization shown in Table I(A) and must therefore be included in the atomic model. Another process leading to overlapping $K\alpha$ features is transitions in atoms that were initially in an excited state populated by the thermal plasma processes. An example is shown in Table I(C). A N-like Al atom with an electron excited into the $n=3$ shell produces a transition in C-like Al after the inner-shell ionization occurs. However, the wavelength of this transition is similar to transitions in B-like Al, since the screening provided by the $3s$ spectator electron induces only a small wavelength shift. The slight redshift of the line due to the extra $n=3$ spectator makes this contribution difficult to distinguish experimentally from transitions in B-like Al, implying that the collisional radiative calculations must account for both the charge state distribution and the excited state distributions within each charge state. These effects—multiple ionization and excited state configurations—are essential to production of $K\alpha$ emission from atoms initially in He-, Li-, and Be-like charge states. The ground configurations of these ions initially have no electrons in the $2p$ state and consequently, either thermal excitation, multiple ionization, or simultaneous ion impact ionization and excitation are required to produce $K\alpha$ satellites. An example for $K\alpha$ production from Be-like Al is shown in Table I(D).

The $K\alpha$ spectra in the present experiments are recorded with an elliptical crystal spectrograph [36] operated in the Johann-focusing mode [37]. This essentially renders source broadening negligible, a crucial consideration since the scale size of the plasma created by the ion beam is ~6–10 mm (Fig. 2). The elliptical geometry also has the advantage that the detector is isolated from the line of sight to the plasma by the structure of the slit placed at the ellipse focus, reducing the debris and scattered x rays incident on the detector. The debris resulting from the large energy delivered to the diode routinely destroys the x-ray crystals used in these experiments, but the detector survives intact. A 1.0 or 2.0 mm space-resolving slit provides 2 or 4 mm spatial resolution at the target (magnification=1). The pentaerythritol (PET) crystal was curved [38] to a 49.2 cm focal-length ellipse with eccentricity typically 0.9188 and height parameter 4.1656 cm (as defined in Ref. [36]). The range covered in first order was 6.4–8.66 Å. The spectral resolution was as high as $\lambda/\delta\lambda \sim 1200$, determined by recording Al $K\alpha$ spectra from a standard x-ray source. Note that the destruction of the x-ray crystals in each experiment prevented calibrations of all crystals used and the actual spectral resolution in the data shown below may have been somewhat lower. The spectra are recorded on Kodak DEF film, developed for 5 min in GBX developer at 68°. The data below are corrected for the film response [39,40] (including the angle of incidence in the Johann geometry), the nominal crystal reflectivity [41], and the light-tight filter transmission.

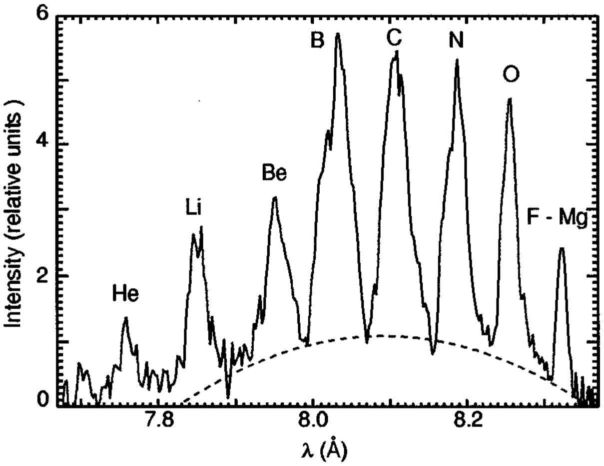

FIG. 3. Al $K\alpha$ x-ray spectrum from PBFA II experiment 5851. The isoelectronic species designations correspond to the Al charge state primarily responsible for the labeled feature.

A typical time-integrated $K\alpha$ spectrum from a foil heated by the PBFA-II Li ion beam consists of $1s$-$2p$ transitions from Mg-like to He-like aluminum (Fig. 3). In Fig. 3 the features are labeled according to the charge state in which the transition actually occurs, after inner-shell ionization takes place. The emission from a given $K\alpha$ satellite at any instant in time depends on the number of target atoms in the appropriate configuration, the number and kinetic energy of the incident projectiles, and the relevant atomic rates. The intensity of each feature in a time-integrated spectrum (Fig. 3) depends on a convolution of the time histories of the target charge state and excited state distributions and the beam current density and kinetic energy. We note that in the absence of large radiation losses, the target temperature increases monotonically as long as the ion beam irradiation is significant. Each change in the target temperature of a few eV induces a perceptible change in the $K\alpha$ spectrum (see Sec. IV). This, plus the fact that the $K\alpha$ emission occurs only when the ion beam is present, means that some information on the time evolution of the target conditions is contained even in time-integrated spectra. A complete analysis of time-integrated data requires the use of a radiation-hydrodynamic calculation, as described below, since the $K\alpha$ intensities are a convolution of both the time-varying beam intensity and the time-varying target conditions. However, the $K\alpha$ features corresponding to low charge states are produced mainly early in time and the features corresponding to high charge states are produced mainly near the end of the pulse, when the temperature is the highest. Thus, even in the absence of time-resolved data, we can determine the approximate peak temperature by comparing the relative intensities of the features arising from the He- and Li-like charge states with collisional radiative equilibrium (CRE) calculations.

The CRE code [15] computes atomic level populations by solving multilevel statistical equilibrium equations self-consistently with the radiation field and ion beam properties. The processes included in the CRE code are described in Refs. [15] and [42] and [43]. The transport of line radiation was computed using a frequency-averaged escape probability model [44,45], while radiation due to the Al continuum self-emission was transported using a multiangle, multifrequency model. Emergent spectra included opacity effects due to bound-bound, bound-free, and free-free processes. Line shapes were modeled using Voigt profiles, with broadening effects due to Doppler, Stark, natural, and Auger broadening included.

The reliability of the CRE calculations was verified by benchmarking [46] against published experimental and theoretical results. Comparisons with laser plasma absorption spectra were used to confirm the accuracy of the level energies, level populations, and oscillator strengths for plasma conditions similar to those encountered here. The portions of the code that are unique to ion-beam-induced emission spectroscopy—namely, the fluorescence yields and inner-shell ionization cross sections—have also been tested as extensively as possible. The fluorescence yield calculations agree to within ±7% with previous calculations [47,48] for Al and Ne plasmas. We expect the present calculations to provide the most accurate results, since the previous work used pure LS [47] and pure JJ [48] coupling. The multiple ionization cross sections are calculated [42] in a similar manner to the well-established methods [49–51] used for cold targets. We verified that the CRE calculations accurately reproduce the available measurements. However, we regard the accuracy of the multiple ionization cross sections as unconfirmed, since the experimental cross sections in the literature are mainly limited to neutral atoms with closed L-shell configurations, while we are mainly concerned with open L-shell Al ions. In order to evaluate the possible impact of errors in the multiple ionization cross sections, we varied the cross section and examined the difference in the temperature that would be inferred from the He-like Al to Li-like Al satellite intensity ratio. We considered two extreme cases. First, the multiple ionization cross sections were set equal to zero. This resulted in a temperature that was higher by about 10%. Second, the single (K), double (KL), and triple (KLL) ionization cross sections were multiplied by factors of 2, 4, and 8, respectively. Larger factors were used for transitions with increasing number of ionizations because of larger uncertainties in the calculated cross sections. In this case, the temperature inferred was ~10% lower than the nominal value. These uncertainties are not included in the temperature uncertainties reported elsewhere in this paper, since there is no hard evidence that suggests the nominal calculations are inaccurate.

The experimental intensity ratio of the He-like to Li-like emission is 0.22±20%. The uncertainty in this ratio mainly arises from the weakness of the He_α feature compared to the spectrum noise, making a precise determination of the background intensity difficult. The relative intensities and the uncertainties are determined by fitting Gaussian peaks to the data using the ROBFIT line-fitting computer code [53]. We have also reduced the measured He_α intensity by 30% to account for blending with a Li-like satellite, measured in higher spectral resolution data described in Sec. V. The peak plasma electron temperature is estimated from CRE calculations of the line ratio as a function of temperature and density. The calculations show that this ratio is very sensitive to changes in target temperature. For example, at an electron density of $2\times10^{20}\ \mathrm{cm}^{-3}$, a change in the electron temperature from 40 to 42 eV causes an approximately factor-of-two change in the He-to-Li ratio. The sensitivity of this ratio to density changes is smaller, but not negligible. At 40 eV, an order of magnitude change in the density produces a factor of two change in the ratio. For the present analysis, we used an electron density range from $8\times10^{19}-8\times10^{20}\ \mathrm{cm}^{-3}$, as suggested by the simulation described below. The plasma electron temperature range consistent with the experimental ratio and in this density range is $T_e=38-43$ eV.

IV. BEAM-TARGET INTERACTION

We used the data to test radiation-hydrodynamic simulations of the ion beam target interaction performed with the BUCKY [54] 1D Lagrangian computer code. The measured ion beam parameters are used as input to the code and the resulting target temperature and density evolution are calculated. The ion beam stopping model is based on a method developed by Mehlhorn [55]. The particle angle of incidence is taken into account using particle-in-cell calculations [56] of the projectile trajectories that include 2D diode geometry effects and the initial 45° target angle. The radiation transport is treated using two models. A multigroup (100 groups) multiangle model is used for the Au bound-bound, bound-free, and free-free radiation, as well as for the continuum radiation in the Al and CH zones. The Au opacities in this model are computed using the unresolved-transition-array model EOSOPA [46], and a detailed configuration accounting model is used for the lower-Z elements. The second model treats the line radiation for the Al and CH using a CRE model embedded within the hydrodynamics code. The CRE model is similar to the stand-alone CRE model described in Refs. [15], [42], and [43], but it uses fewer levels and an escape probability model to reduce computation time. This model includes resonant self-absorption effects and calculates the self-consistent non-LTE atomic level populations using 222 Al, 43 C, and 4 H levels. The results of the hydrodynamic simulations are postprocessed using the stand-alone CRE code since greater atomic physics detail is required to generate accurate spectra than for computing the populations and charge state distributions needed for the plasma evolution. The time-integrated synthetic spectrum for comparison with the data is compiled by summing the computed spectra over time.

In our simulations it was found that the temperature in the Al layer at late times was significantly suppressed due to

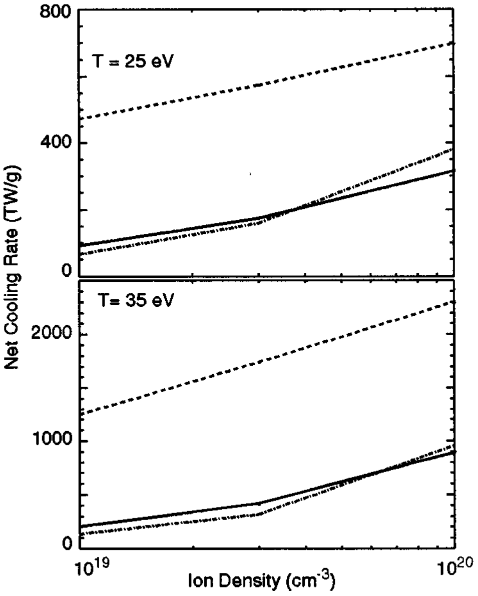

FIG. 4. Radiative cooling rate for an Al plasma, calculated with three different models. The solid curve is from the stand-alone CRE code and is considered to be the most accurate. The dot-dashed curve is from the smaller CRE model embedded within the BUCKY radiation-hydrodynamics code. The dashed curve is from a multigroup radiation transport model, which does not adequately treat resonant self-absorption. The pre-expansion plasma thickness in all cases was taken to be 2000 Å.

radiation losses. Because of this, a considerable effort was made to accurately model and benchmark the Al radiation physics within the radiation-hydrodynamic code. Note that a similar treatment of detailed radiation physics has been utilized by others [57,58] for higher-temperature laser-produced plasmas. Figure 4 shows a comparison of the net radiative cooling rate for an Al plasma computed using three models. The solid curve was computed using our stand-alone CRE model. In this calculation a multiangle, multifrequency model, resolving the line profiles in frequency space and including line overlap, was used to treat the radiative transfer. This calculation, which we consider to be the most accurate of the three models, indicates that many of the strongest lines are optically thick, and are therefore prone to resonant self-absorption effects. The continuum, however, is optically thin over most of the spectrum. The dot-dashed curve in Fig. 4 corresponds to the Al cooling rates calculated using the CRE–line transport model embedded in the radiation-hydrodynamics code. In this case, each line was transported using a single frequency-averaged opacity in an escape probability model, but with a similar level of detail in the atomic energy level modeling. Note the good agreement between this model and the stand-alone CRE results. The dashed curve in Fig. 4 corresponds to the radiative cooling rates computed using a ''multigroup'' model, in which line opacities and emissivities are grouped into a relatively small number of frequency bins (100 groups) and transported along with the continuum. Thus, in this model the detailed frequency structure is to a large degree lost, and resonant self-absorption effects are not properly accounted for. The radiative cooling rates computed using this more ''traditional'' approach to radiative transfer are roughly a factor of 2–5 higher than those of the more detailed calculations for these plasma conditions. Because the multigroup opacities were computed using an atomic model with the same level of detail as the stand-alone CRE code, the differences are due entirely to the fact that the multigroup transport algorithm does not adequately treat resonance self-absorption effects. Thus, a detailed treatment of line radiation transfer effects is required in our analysis and, in general, this approach should be considered for any target calculation where optically thick lines but optically thin continuum radiation is encountered.

The actual ion beam incident on the target at any instant has an approximately-Gaussian 2D distribution of intensities. The width of the distribution changes as the focal spot size changes in time (Fig. 2). Thus, the $K\alpha$ spectrum at any instant is a sum of emission from regions that have ben heated by different beam intensity histories and that are experiencing different beam current densities at that instant. In order to approximate this complex situation with 1D simulations, we divided the target into five different spatial regions ranging from the central, most intense, part of the beam down to the less intense beam wings. The central region is an ellipse with 1.08 mm minor and 2.3 mm major radii, chosen such that the average irradiance during the early part of the beam pulse was 97% of the peak irradiance shown in Fig. 2. The surrounding regions are successively larger elliptical annuli, corresponding to lower irradiance values as the location is further removed from the most intense part of the beam focal spot. We derived the beam irradiance history incident on each region from the Rutherford-scattering data and performed a separate 1D simulation for each region. We then postprocessed the results to obtain a synthetic spectrum from each simulation, and combined the spectra together using weighting appropriate to the areas.

The deposition of beam energy and the reradiation of that energy within the Au and Al target layers is shown in Fig. 5. The results in Fig. 5 correspond to the central simulation ellipse. The beam specific deposition in the Al peaks at 435 TW/g, compared to about 150 TW/g for the Au layer. The peak in the deposited power occurs about 2 ns later than for the incident power, because as the target is heated, the value of dE/dx increases. At peak incident power (12 ns) the enhancement of the deposited power over the value expected for room temperature materials is approximately 2.4 and 2.0 for the Al and Au, respectively. At 30 ns the target temperature is higher and the enhancements are 4.5 and 3.1, respectively. Note that the total power deposited in the Au region is actually higher than for the Al because of the higher Au density. The radiation terms are determined by averaging over all the zones within each layer and dividing by the mass. The Au radiation quickly becomes optically thick for both the lines and the continuum. The net radiation loss grows correspondingly quickly and is comparable to the ion beam heating after about 15 ns. Conversely, the Al layer never has appreciable continuum opacity, although the optical depths for some of the lines are large. Note that here we are referring to the thermally excited transitions (e.g., $2s$-$2p$ and $2p$-$3d$) that dominate the radiation losses, while the nonthermal ion-beam-produced $K\alpha$ transitions provide diagnostic information. There is a brief period around $t=10$ ns when absorption of Au radiation by the Al is sufficient to provide net radiation heating of the Al. Later, the radiation

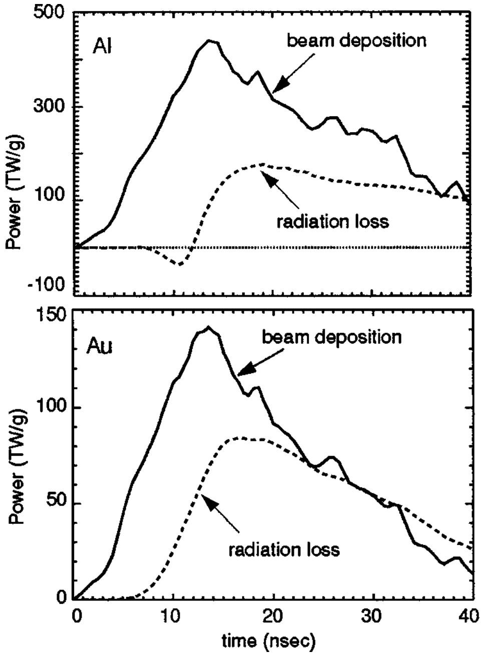

FIG. 5. Power balance calculated with the BUCKY radiation-hydrodynamic code, using the beam parameters shown in Fig. 2 as input. The results shown are region averages over the Al and Au zones. The solid curve is the ion beam deposition and the dashed curve is the net radiation loss.

losses dominate the radiation heating, but the radiation loss does not become comparable to the ion beam heating until the end of the pulse.

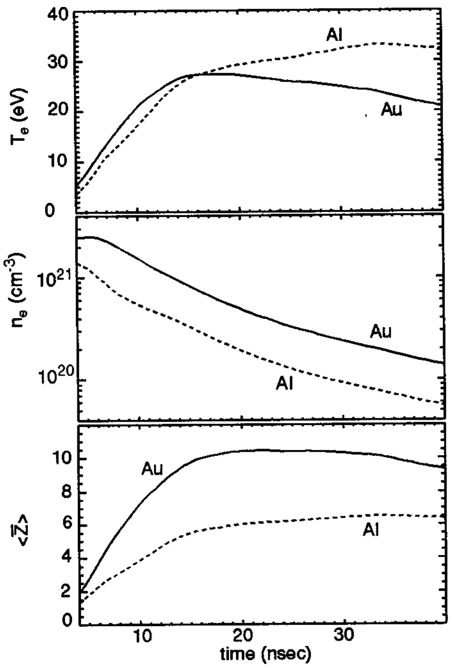

FIG. 6. Region-averaged electron temperature, electron density, and $\bar{Z}$ calculated with BUCKY computer simulation for the PBFA II 5851 conditions. The solid curves refer to the Au region and the dashed curves refer to the Al.

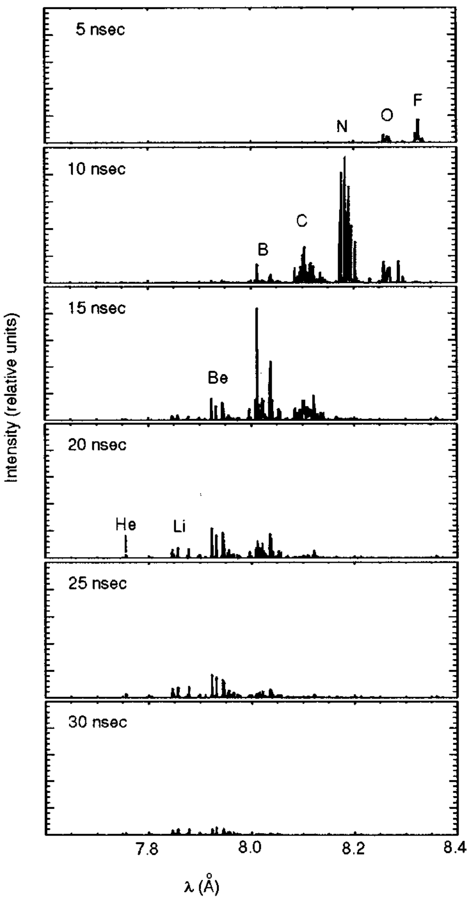

FIG. 7. Temporal evolution of the spectral emission calculated by postprocessing the simulation results for PBFA II experiment 5851 with the CRE code.

The evolution of the layer-averaged temperatures, densities, and mean ionization stage $(\bar{Z})$ are shown in Fig. 6. The results in this figure again correspond to the central simulation ellipse. The Au layer initially heats quickly in response to the ion beam heating, reaching a maximum electron temperature of $T_e=27$ eV. However, as the radiation losses grow and the region expands, the Au plasma electron temperature drops. The Au region expands by an average factor of about 4000 during the pulse, reaching an ion density of about 1.5×10^{19} cm^{-3}. In contrast to the Au, the Al plasma electron temperature grows throughout the pulse. The ion beam heating dominates the combined radiation and hydrodynamic-expansion cooling rates. The peak Al electron temperature reaches $T_e=32$ eV, about 16–26% lower than the estimate obtained above using the He- to Li-like ratio. This discrepancy is discussed below.

The temporal evolution of the synthetic spectra obtained by postprocessing the simulation results is shown in Fig. 7. As expected, the emission from the lower charge states occurs mainly during the beginning of the pulse and the higher charge state emission occurs later, after the target temperature has risen substantially. A comparison of the experimental spectrum with the time-integral of the baseline simulation spectra is shown in Figs. 8(a) and 8(b). A more quantitative comparison is obtained by integrating over the appropriate synthetic spectrum wavelength interval to determine the intensity of the main $K\alpha$ features. The intervals used are depicted with arrows in Fig. 8. The intensity of the corresponding experimental features is determined by fitting Gaussian

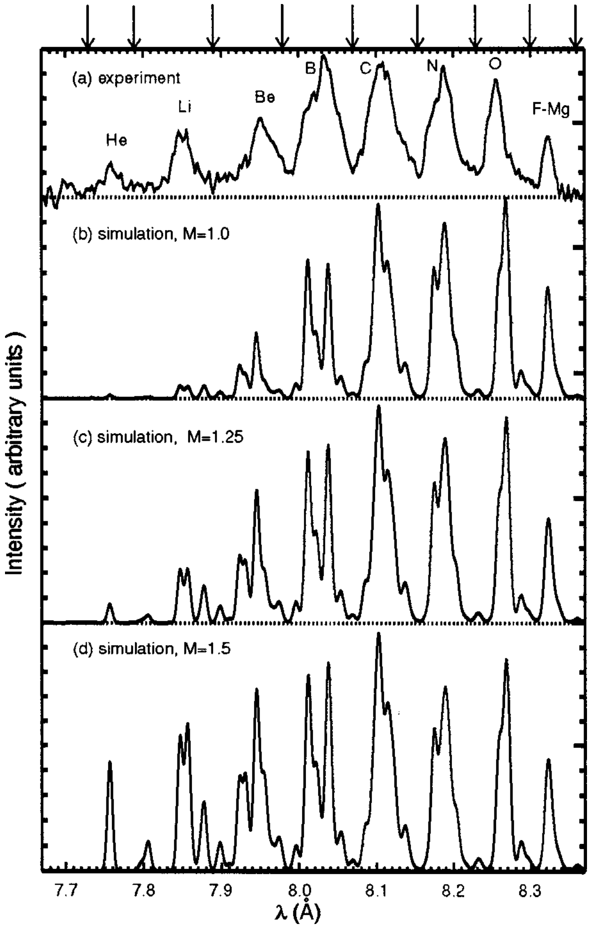

FIG. 8. Comparison of PBFA II 5851 experimental spectrum (a) with synthetic spectra. M is the multiplier on the measured ion beam irradiance used as input to the simulation. The synthetic spectrum in (b) ($M=1.0$) corresponds to the nominal measured beam irradiance while the spectra in (c) and (d) used beam irradiance values that were 25% and 50% higher than the measured value, respectively. The charge state primarily responsible for each $K\alpha$ feature is indicated on the experimental spectrum. The downward arrows at the top of the figure indicate the wavelength intervals used to determine the relative emission intensities shown in Fig. 9.

peaks to the data using ROBFIT [53]. The comparison is displayed in Fig. 9. The experimental and simulation relative intensities are represented by solid and dashed histograms, respectively. The relative intensities have been normalized so that the total intensity equals 1.0. Above each feature is a number that gives the ratio of the simulation to experimental relative intensity. The main features of the experiment are reproduced reasonably well, although the He- and Li-like features in the synthetic spectrum are too weak. This clearly results from the discrepancy noted above: the peak temperature attained in the simulation is lower than the value obtained using the experimental line ratio and the CRE code. In addition, the emission from the C- through F-like features in the simulation is too bright by 20–100%. As pointed out above, the time-integrated intensity of each $K\alpha$ feature depends on the elapsed time that the plasma spends in the temperature-density regime that favors production of that feature, as well as the beam intensity and kinetic energy during that time interval. The extra intensity in the synthetic spectrum low-charge-state features is presumably because

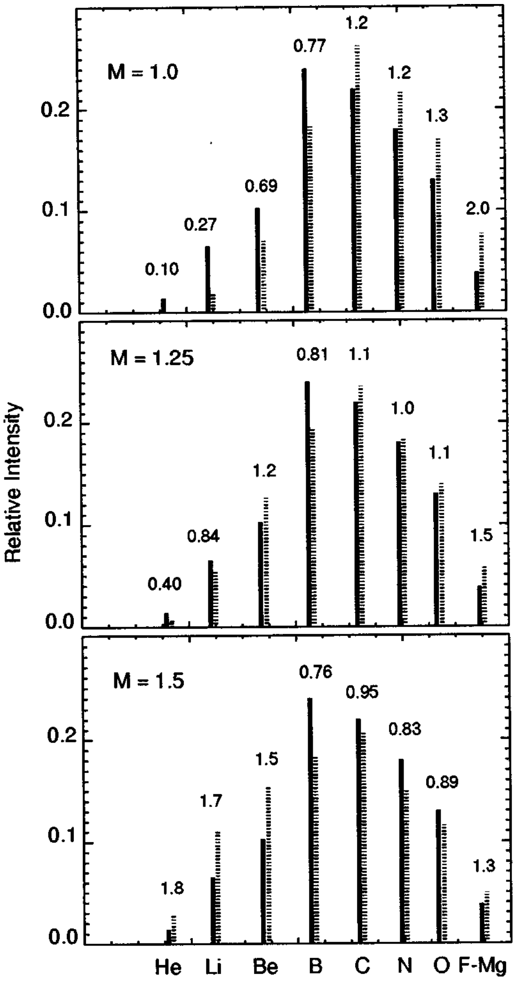

FIG. 9. Relative emission intensities for the $K\alpha$ features in the PBFA II 5851 experiment (solid lines) compared to simulation results (dashed lines). M is the simulation beam intensity multiplier as defined for Fig. 8. The relative emission intensities are normalized so that the total equals one. The number at the top of each feature is the ratio of the simulation value to the experimental value.

the simulation temperature initially rises too slowly, increasing the dwell time for production of low-charge-state features at the expense of the higher charge states. These discrepancies are discussed below.

The agreement between the synthetic and experimental spectra is reasonable considering the approximations that have been made. Three other similar experiments were analyzed with a somewhat simplified atomic model embedded within the radiation hydrodynamics code. Similar results were obtained in all cases: there is generally reasonable agreement, but the synthetic spectrum contains extra intensity from the lower charge states and weak emission from the higher charge states. This systematic trend prompted us to consider what effects might be responsible for the discrepancies. For this purpose we divided our procedure into four categories: the ion beam measurements, the BUCKY code that calculates the temperature-density evolution, the CRE code used to generate synthetic spectra from the BUCKY results, and the recording of the experimental spectrum. The relative intensities in the experimental spectrum are affected by the wavelength dependence of the light-tight filter, the geometry dependence of the instrument sensitivity, the crystal reflectivity, and the film response. Although the instrument used in these experiments was uncalibrated, we are relaying on well-established previous work and consider it unlikely that uncertainties in the experimental spectrum are responsible for the apparent overionization of the synthetic spectra. In addition, the benchmarking described above indicates that the CRE code can accurately reproduce the main $K\alpha$ features observed in the experiment and is not responsible for the underionized synthetic spectra. The impact of the ±30% uncertainty in the ion beam intensity and uncertainties in the ion beam deposition and radiation models within the BUCKY code are essentially inseparable, since a higher plasma temperature would result from higher beam irradiance, larger ion beam stopping power, lower radiation cooling, or some combination of the three. In order to evaluate the possible impact of these effects additional simulations were performed using an enhanced beam current density. The synthetic spectra obtained by boosting the input beam intensity by 25% and 50% are shown in Figs. 8(c) and 8(d), respectively. Histograms of the relative emission intensities are shown in Fig. 9. The simulation with a beam intensity enhancement of 25% gives the best overall agreement, although the simulation He_α intensity is still only 40% of the experimental value. The simulation with the 50% enhancement is overionized, with emission that is too bright from the He-, Li-, and Be-like charge states. The 25% enhancement of the beam intensity is consistent with the estimated ±30% uncertainty in the ion beam irradiance. However, as noted above, this agreement could be obtained by enhancing the beam deposition or by decreasing the radiation losses. The present results demonstrate that our integrated model of the beam deposition, radiation emission and transport, and hydrodynamic expansion is valid within the experimental uncertainties.

V. DISCUSSION AND CONCLUSIONS

The stand-alone CRE code has been benchmarked [46] against laser plasma absorption spectra and it adequately reproduces the main characteristics of the $K\alpha$ spectrum in the present experiment. However, there are some discrepancies that appear to be unique to the ion-excited $K\alpha$ emission spectrum. An experimental spectrum recorded with somewhat higher spectral resolution makes these discrepancies especially apparent (Fig. 10). The notation for the Li-like satellites is described in Ref. [52]. The calculations displayed in Fig. 8 predict an easily discernible splitting of the B-like feature that is not observed in the experiment. In addition, the atomic model underpredicts the intensity of the feature that appears at 7.77 Å in the experimental spectrum, approximately 13 mÅ to the long wavelength side of He_α. This feature appears in two experiments recorded with higher spectral resolution and it has appeared in prior higher-temperature laser-produced spectra [52,59]. It has been tentatively identified as a $1s$-$2p$ transition with a $3s$ spectator electron. This transition is included in the CRE model, but the excited state population is inadequate to explain the experimental intensity. This satellite is merged with the He_α resonance line in the lower-resolution Fig. 3 spectrum. Based on the Fig. 10 spectrum, we estimate that 30% of the apparent He_α intensity in the lower resolution experimental spectrum (Fig. 3) is actually due to this satellite. As mentioned above, this extra intensity was subtracted from the He_α intensity before using the He- to Li-like line ratio to infer the temperature, and it was also subtracted from the experimental intensity in the Fig. 9 histograms. Another important discrepancy is the broad quasicontinuum hump under the lower charge state features, indicated with a dotted line in Figs. 3 and 10. This quasicontinuum does not appear in the synthetic spectra. It is plausible that the quasicontinuum hump arises from merging of many weak transitions with a variety of wavelengths. Such emission can result from transitions with $n=3$ spectator electrons since the $n=3$ spectators induce small wavelength shifts (see Table IC). As noted above, these transitions are included in the CRE model, but the excited state populations in the model are evidently too low.

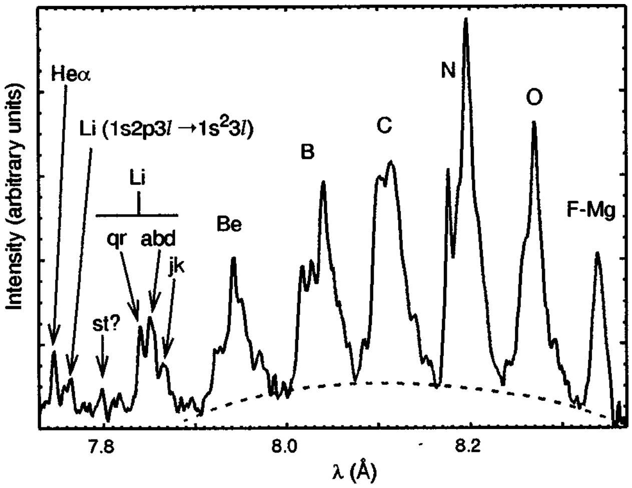

FIG. 10. $K\alpha$ spectrum from PBFA II experiment 6347, recorded with higher spectral resolution than in Fig. 3.

The three discrepancies described above (the B-like satellite profile, the satellite 13 mÅ from He_α, and the quasicontinuum hump) all can be explained by a population mechanism missing from the CRE code, although the splitting in the theoretical B-like profile may also be due to inaccuracies in the theoretical wavelengths. One population mechanism that is under investigation is simultaneous ion-beam-induced excitation and ionization events that could lead to $1s$-$2p$ inner shell transitions with an $n=3$ spectator. Such events are not included at present because a reliable method for calculation of the cross sections is unavailable. Another possibility is that the discrepancies are a reflection of assumptions made in the treatment of ion stopping in plasmas. Although we include the nonthermal processes associated with ion beam-impact ionization in the CRE modeling, we assume that the electron distribution is Maxwellian. The Maxwellian temperature is obtained from the radiation-hydrodynamics calculations, based on the ''stopping power'' model [55]. In reality, it is possible that the ''stopping power'' process (i.e., ion beam–target electron collisions) leads to a non-Maxwellian electron distribution in the target. The subsequent interaction of the nonthermal electrons with the atoms in the plasma can then lead to production of $K\alpha$ satellites with $n=3$ spectator electrons. For example, dielectronic recombination is known to populate the levels of interest, but it requires that the energy of the colliding electron be greater than 1.4 keV in order to produce the satellite on the long wavelength side of He_α. Note that these nonthermal processes cannot entirely explain the underionization of the synthetic spectrum because the production of the observed He-, Li-, and Be-like intensities would still require higher thermal temperatures than achieved in the radiation-hydrodynamics simulations.

The present level of agreement between the data and simulations is encouraging, especially considering the lack of prior benchmarking experiments that could be used to test the simulations. However, even though the expected cost of a light-ion fusion facility is expected [1] to be low compared to other approaches, it is still high enough that experimental confirmation of accurate predictive capability for beam plasma interaction is a prerequisite to serious consideration. Therefore, more stringent tests of beam-plasma interaction models are required. Limitations in the present experiment include ±30% accuracy in the beam irradiance, averaging of the spectrum over both time and space, and the possible impact of beam nonuniformities. The target temperature has an uncertainty due to the density dependence of the spectra and the lack of an independent density diagnostic. This forces us to rely somewhat on the simulations that we are trying to test. The latter problem can be eliminated in future experiments by simultaneously recording spectra from two separate elements with different temperature and density sensitivities (e.g., Al and Mg). In the present experiments the effect of integrating over temporal and spatial gradients is ameliorated by the fact that the spectral emission is directly induced by the ion beam, enabling some tests of the time-dependent simulation fidelity using time-integrated data. However, acquisition of time-resolved spectra would clearly provide a better test. The extension of $K\alpha$ spectroscopy to diagnose ion-heated targets using the target self-emission and the demonstration that simultaneous Rutherford-scattering beam diagnostics are compatible with spectroscopic target-heating measurements paves the way for future improved experiments. Using the present results as a guide, we are designing more ideal experiments using multiple elements, time-resolved spectroscopy, improved beam intensity measurements, and dot spectroscopy [60] to reduce effects of gradients.

ACKNOWLEDGMENTS

The authors thank the PBFA II operations crew for assistance with the experiments and D. L. Cook, R. J. Leeper, and J. P. Quintenz for continuous support and encouragement. We are grateful to A. B. Filuk and Y. Maron for reading the manuscript. This work was supported by the U.S. Department of Energy under Contract No. DE-AC04-94AL85000. Sandia is a multiprogram laboratory operated by Sandia Corporation, a Lockheed Martin Company, for the U.S. Department of Energy.

---

[1] J. P. VanDevender and D. L. Cook, Science **232**, 831 (1986).

[2] J. P. Quintenz *et al.*, in *Proceedings of the 15th International Conference on Plasma Physics and Controlled Nuclear Fusion Research* (IAEA, Seville, 1994), Vol. 3, p. 39.

[3] J. P. VanDevender and H. Bluhm, *Nuclear Fusion by Inertial Confinement*, edited by G. Vellarde, Y. Ronen, and J. M. Martinez-Val (CRC Press, Ann Arbor, 1993), p. 455.

[4] S. A. Slutz (private communication); Laser Part. Beams **13**, 243 (1995).

[5] T. A. Mehlhorn *et al.*, *Laser Interaction and Related Plasma Phenomena* (Plenum Press, New York, 1992), Vol. 10, p. 553.

[6] Z. Zinamon, *Nuclear Fusion By Inertial Confinement*, edited by G. Vellarde, Y. Ronen, and J. M. Martinez-Val (CRC Press, Ann Arbor, 1993), p. 119.

[7] D. H. H. Hoffman *et al.*, Z. Phys. A **30**, 339 (1988).

[8] D. Gardes *et al.*, Europhys. Lett. **8**, 701 (1988).

[9] C. Stoekl (private communication).

[10] F. C. Young *et al.*, Phys. Rev. Lett. **49**, 549 (1982).

[11] J. N. Olsen *et al.*, J. Appl. Phys. **58**, 2958 (1985).

[12] J. Jacoby *et al.*, Phys. Rev. Lett. **65**, 2007 (1990).

[13] G. E. Belyaev *et al.*, Laser Part. Beams **10**, 737 (1992).

[14] J. Bailey *et al.*, Laser Part. Beams **8**, 555 (1990).

[15] J. J. MacFarlane *et al.*, Phys. Rev. E **47**, 2748 (1993).

[16] G. A. Chandler *et al.*, Rev. Sci. Instrum. **63**, 4828 (1992).

[17] M. S. Derzon *et al.*, Phys. Rev. Lett. **76**, 435 (1996).

[18] D. J. Johnson *et al.*, in *Proceedings of the 7th IEEE Pulsed Power Conference, Monterey, CA*, edited by R. White and B. H. Bernstein (IEEE, New York, 1989), p. 944.

[19] R. J. Leeper *et al.*, Rev. Sci. Instrum. **59**, 1860 (1988).

[20] W. A. Stygar *et al.*, Rev. Sci. Instrum. **59**, 1703 (1988).

[21] W. A. Stygar *et al.*, Rev. Sci. Instrum. **63**, 4860 (1992).

[22] L. P. Mix *et al.*, Rev. Sci. Instrum. **63**, 4863 (1992).

[23] R. J. Leeper *et al.*, in *Fast Electrical and Optical Diagnostic Principles and Techniques*, Vol. 1 of *NATO Advanced Studies Institute Series E: Applied Sciences*, edited by J. E. Thompson and L. H. Luessen (Martinus Nijhoff, Amsterdam, 1986), pp. 263–359.

[24] R. J. Leeper *et al.*, J. Appl. Phys. **60**, 4059 (1986).

[25] R. J. Leeper *et al.*, in *Proceedings of the 8th International Conference on High Power Particle Beams*, edited by B. N. Breitzman and B. A. Knyazev (World Scientific, New York, 1990), p. 173.

[26] L. L. House, Astrophys. J., Suppl. Ser. **18**, 21 (1969); P. Beiersdorfer *et al.*, Astrophys. J. **409**, 846 (1993).

[27] J. D. Hares, J. D. Kilkenny, M. H. Key, and J. G. Lunney, Phys. Rev. Lett. **42**, 1216 (1979).

[28] N. H. Burnett *et al.*, Phys. Rev. A **29**, 2294 (1984).

[29] E. Nardi and Z. Zinamon, J. Appl. Phys. **52**, 7075 (1981).

[30] S. J. Davidson *et al.*, Appl. Phys. Lett. **52**, 847 (1988).

[31] C. Chenais-Popovics *et al.*, Phys. Rev. A **40**, 3194 (1989).

[32] T. S. Perry *et al.*, Phys. Rev. Lett. **67**, 3784 (1991).

[33] R. C. Mancini, C. F. Hooper, Jr., and R. L. Coldwell, J. Quant. Spectrosc. Radiat. Transf. **51**, 201 (1994).

[34] T. S. Perry *et al.*, J. Quant. Spectrosc. Radiat. Transf. **54**, 317 (1995).

[35] J. D. Garcia, R. J. Fortner, and T. M. Kavanagh, Rev. Mod. Phys. **45**, 111 (1973).

[36] B. L. Henke, H. T. Yamada, and T. J. Tanaka, Rev. Sci. Instrum. **54**, 1311 (1983).

[37] B. A. Hammel, D. W. Phillion, and L. E. Ruggles, Rev. Sci. Instrum. **61**, 1920 (1990).

[38] X-Ray Optics, Inc., Jacksonville, FL 32216.

[39] B. L. Henke *et al.*, J. Opt. Soc. Am. B **3**, 1540 (1986).

[40] P. D. Rockett *et al.*, Appl. Opt. **24**, 2536 (1985).

[41] B. L. Henke (private communication).

[42] P. Wang, J. J. MacFarlane, and G. A. Moses, Laser Part. Beams **13**, 191 (1995).

[43] P. Wang, Phys. Rev. E **48**, 3934 (1993).

[44] J. P. Apruzese *et al.*, J. Quant. Spectrosc. Radiat. Transf. **23**, 479 (1980).

[45] J. P. Apruzese, J. Quant. Spectrosc. Radiat. Transf. **34**, 447 (1985).

[46] J. J. MacFarlane *et al.*, Laser Part. Beams **13**, 231 (1995).

[47] F. Combet Faroux, J. Phys. (Paris) Colloq. **48**, C9-199 (1987).

[48] M. H. Chen and B. Crasemann, Phys. Rev. A **12**, 959 (1975).

[49] J. H. McGuire and P. Richard, Phys. Rev. A **8**, 1374 (1973).

[50] J. M. Hansteen and O. P. Hosebekk, Phys. Rev. Lett. **29**, 1361 (1972).

[51] R. L. Watson *et al.*, J. Phys. B **16**, 835 (1983).

[52] V. A. Boiko, A. Ya. Faenov, and S. A. Pikuz, J. Quant. Spectrosc. Radiat. Transf. **19**, 11 (1978).

[53] R. L. Coldwell and G. J. Bamford, *The Theory and Operation of Spectral Analysis Using ROBFIT* (AIP, New York, 1991).

[54] J. J. MacFarlane, G. A. Moses, and R. R. Petersen (unpublished).

[55] T. A. Mehlhorn, J. Appl. Phys. **52**, 6522 (1981).

[56] T. A. Haill (unpublished).

[57] J. Davis, K. G. Whitney, and J. P. Apruzese, J. Quant. Spectrosc. Radiat. Transf. **20**, 353 (1978).

[58] D. Duston and J. Davis, Phys. Rev. A **23**, 2602 (1981).

[59] O. Renner *et al.*, Laser Part. Beams **12**, 539 (1994).

[60] M. J. Herbst *et al.*, Rev. Sci. Instrum. **53**, 1418 (1982).